# Structure, Defects and Microwave Dielectric Properties of Al-Doped and Al/Nd Co-doped $Ba_4Nd_{9.33}Ti_{18}O_{54}$ Ceramics

**Weijia Guo** ( guoweijia0315@163.com )
Tsinghua University https://orcid.org/0000-0003-2481-3527
**Zhiyu Ma**
Tsinghua University
**Yu Luo**
Tsinghua University
**Yugu Chen**
Tsinghua University
**Zhenxing Yue**
Tsinghua University
**Longtu Li**
Tsinghua University

---

**Research Article**

**Keywords:** microwave dielectric ceramics, Ba4Nd9.33Ti18O54, Al and Al/Nd doping, structural and defect modulation

**Posted Date:** September 17th, 2021

**DOI:** https://doi.org/10.21203/rs.3.rs-783511/v2

---

# Abstract

Low-loss tungsten-bronze microwave dielectric ceramics are a kind of dielectric materials with potential application value for miniaturized dielectric filters and antennas in 5G communication technology. In this work, a novel Al/Nd co-doping method of $Ba_4Nd_{9.33}Ti_{18}O_{54}$ (BNT) ceramics with a chamical formula of $Ba_4Nd_{9.33+z/3}Ti_{18-z}Al_zO_{54}$ (BNT-AN, $0 \leq z \leq 2$) was proposed to improve the dielectric properties through structural and defect modulation. Together with Al-doped ceramics ($Ba_4Nd_{9.33}Ti_{18-z}Al_{4z/3}O_{54}$, BNT-A, $0 \leq z \leq 2$) for comparison, the ceramics were prepared by solid state method. It is found that Al/Nd co-doping method has a significant effect on improving the dielectric properties compared with Al doping. As the doping amount $z$ increased, the relative dielectric constant ($\varepsilon_r$) and the temperature coefficient of resonant frequency ($\tau_f$) of the ceramics decreased, and the $Q\times f$ values of the ceramics obviously increased when $z \leq 1.5$. Excellent microwave dielectric properties of $\varepsilon_r = 72.2$, $Q\times f = 16480$ GHz, and $\tau_f = +14.3$ ppm/℃ were achieved in BNT-AN ceramics with $z = 1.25$. Raman spectroscopy and thermally stimulated depolarization current (TSDC) technique were firstly combined to analyze the structure and defects in the dielectric ceramics. It is shown that the improvement on $Q\times f$ values were origined from the decrease in the strength of the $A$-site cation vibration and the concentration of oxygen vacancies ($V_{\ddot{o}}$), demonstrating the effect and mechanism underlying for structural and defect modulation on the performance improvement of microwave dielectric ceramics.

# 1 Introduction

Nowadays, the fifth-generation telecommunication (5G) technology has been developing rapidly, in which ceramic materials could play an important role [1]. Microwave dielectric ceramics with high $Q\times f$ value ($Q = 1/\tan\delta$, and $f$ is the resonant frequency) and excellent temperature stability are widely used to manufacture 5G antennas and filters [2–5]. In order to meet the requirements of device miniaturization, microwave dielectric ceramics having medium/high relative dielectric constant ($\varepsilon_r$) have been a focus of research [6], including $TiO_2$ [7, 8], $Ba_{6-3x}Ln_{8+2x}Ti_{18}O_{54}$ (BLT, where Ln = rare earth element) [9, 10], $CaO$-$Li_2O$-$Ln_2O_3$-$TiO_2$ [11, 12], $Ca_{1-x}Ln_{2x/3}TiO_3$ (CLT) [13–15], lead-based perovskite [16, 17], etc. In recent years, BLT with a tungsten-bronze structure and CLT with a perovskite structure have been extensively studied [18–23]. Meanwhile, novel ceramic systems such as $Bi_2(Li_{0.5}Ta_{1.5})O_7$ [24, 25] and $BiVO_4$ [26, 27] have also been developed. However, the above-mentioned ceramic materials either have a relatively low $Q\times f$ value or a relatively large temperature coefficient of resonant frequency ($\tau_f$), which cannot yet meet the application needs of 5G technology. It is necessary to develop microwave dielectric ceramics with better comprehensive performance.

The crystal structure of BLT ceramics is composed by three types of large cation sites: $A1$ rhombic sites, $A2$ pentagonal sites, and $B$ sites (occupied by $Ti^{4+}$) in the center of $TiO_6$ octahedra [10]. According to Ohsato's report [10], $Ln^{3+}$ and $Ba^{2+}$ respectively occupy the $A1$ and $A2$ sites when $x = 2/3$, and the ordering of $Ln^{3+}$ and $Ba^{2+}$ reduces the internal strain and leads to the largest $Q\times f$ value. To further improve the $Q\times f$

value of BLT ceramics, a large amount of doping modification research was displayed, especially the substitution of low-valence cations for $Ti^{4+}$ at the *B* sites. Chen et al. [28] and Tao et al. [29] replaced $Ti^{4+}$ with the same amount of $Al^{3+}$ to improve the $Q\times f$ value, while the condition of charge balance was not achieved. In order to meet the condition of charge balance, one method was using composite ions such as $(Cr_{1/2}Nb_{1/2})^{4+}$, $(Mg_{1/3}Nb_{2/3})^{4+}$ or $(Al_{1/2}Nb_{1/2})^{4+}$ to substitute $Ti^{4+}$ [30–32], yet it complicated the synthesis process. The other method is using excessive trivalent cations (4/3 times in stoichiometry) such as $Cr^{3+}$, $Al^{3+}$ or $Ga^{3+}$ to substitute $Ti^{4+}$ [33–36], yet none of the studies have explained which site these cations entered. Considering that the *A*1 sites of BLT structure are usually not fully filled, the excessive cations might enter the *A*1 sites. However, the radii of those cations are much smaller than the size of the *A*1 sites, which might affect the stability of the crystal lattice and lead to the deterioration of the $Q\times f$ value. Therefore, it is important to conduct a further study on the ion occupancy during these doping process.

In the present study, a new strategy, i. e. Al/Nd co-doping in $Ba_4Nd_{9.33}Ti_{18}O_{54}$ (BNT) ceramics, is proposed to improve the dielectric properties of tungsten-bronze microwave dielectric ceramics through structural and defect modulation, in which the condition of charge balance was maintained by using the same amount of $Al^{3+}$ to substitute $Ti^{4+}$, and adding $Nd^{3+}$ to fill the vacancies at the *A*1 site simultaneously, with a chamical formula of $Ba_4Nd_{9.33+z/3}Ti_{18-z}Al_zO_{54}$ (BNT-AN, $0 \le z \le 2$). Correspondingly, $Ba_4Nd_{9.33}Ti_{18-z}Al_{4z/3}O_{54}$ (BNT-A, $0 \le z \le 2$) ceramics are also prepared for comparison. The theoretical solid solubility should reach when $z = 2$, at which the vacancies at the *A*1 site could be completely filled. Rietveld refinement, Raman spectroscopy and thermally stimulated depolarization current (TSDC) are applied to analyze the crystal structure and the strength of the *A*-site cation vibration. Microwave dielectric ceramics with better comprehensive performance are obtained through Al/Nd co-doping, and the relationship between the structure and the microwave dielectric properties of the ceramics is discussed in the present paper.

## 2 Experimental Procedure

The BNT-A and BNT-AN ceramics were prepared through the traditional solid-state processing. High-purity powders including $BaCO_3$ (99.8%, Alfa Aesar), $Nd_2O_3$ (99.9%, Aladdin), $TiO_2$ (99.99%, Macklin), and $Al_2O_3$ (99.99%, Aladdin) were used as the raw materials. All the raw powders were calcined at 600 °C for 4 hours, weighed according to the stoichiometric composition and ball milled for 4 hours in ethanol. After drying, the mixture was calcined at 1150 °C for 4 hours, then re-milled and dried. The dried powders were ground with polyvinyl alcohol solution (PVA, 5 wt%) and uniaxially pressed into cylinders with a diameter of 10 mm and an appropriate thickness. Finally the specimens were preheated at 600 °C for 4 hours to remove the binder and sintered in the range of 1350 °C and 1550 °C for 4 hours.

The surfaces of the sintered ceramics were observed by scanning electron microscopy (SEM; MERLIN VP Compact, Carl Zeiss, Germany). The phase compositions and crystal structures of the ceramics were analyzed by X-ray diffraction (XRD; D8 Advance, Bruker, Karlsruhe, Germany) with Cu Kα radiation.

Rietveld refinement were executed using the FullProf program [37] with XRD data collected over a 2θ range of 10°~120°. The bulk densities of the ceramics were determined by the Archimedes method, and the relative densities were calculated by the measured and theoretical ones. The $\varepsilon_r$ and $\tau_f$ values at microwave range were measured using the Hakki-Coleman method [38] by exciting the $TE_{011}$ resonant mode [39] using a vector network analyzer (HP8720ES, Hewlett-Packard, Santa Rosa, CA, USA). The $Q\times f$ values were measured using the $TE_{01\delta}$ mode in the cavity method [40]. Raman spectra (20 ~ 1200 $cm^{-1}$) of the ceramics were measured on a high-resolution Raman spectrometer (LabRAM HR800, Horiba Jobin-Yvon, France) with the existing line at 523 nm of a Nd/YAG laser at room temperature.

TSDC measurements were accomplished using a pA meter (6517B, Keithley, Cleveland, OH), and the temperature was controlled by a quarto temperature controller of Novocontrol Technologies (Montabaur, Germany). The ceramic pellets were polished and gold electrodes were sputtered on both sides. The specimens were initially polarized under a dc electric field ($E_p$) at a constant temperature ($T_p$) for a period of time $t_p$ (100 V/mm $\leq E_p \leq$ 350 V/mm, $T_p$ = 300 °C, $t_p$ = 10 minutes), then rapidly cooled to -100 °C with $E_p$ maintained to freeze the polarized defects. After $E_p$ removed and being short-circuited for 10 minutes, the specimens were heated to 300 °C with a constant heating rate of 5 °C/min, with the depolarization currents continually recorded.

# 3 Results And Discussion

Figure 1 presents the SEM photographs of the surface morphology of the ceramic samples. All BNT-A and BNT-AN samples show a single phase of rod-like grains. As shown in Fig. 1(a)-(c), BNT-A ceramics with different $z$ values could be well-sintered at 1400 °C, indicating that the sintering temperature of the BNT-A ceramics is stable at around 1400 °C, and basically does not change with the doping amount. In comparison, BNT-AN ceramics with $z$ = 2 are well-sintered at 1550 °C as shown in Fig. 1(f), illustrating that the sintering temperature of the BNT-AN ceramics increases with increasing doping amounts. Figure 1(d)(e) show that the grain size of the ceramics with the same composition becomes larger as the sintering temperature gets higher.

The XRD patterns of the ceramic samples are shown in Fig. 2. All samples can be confirmed as a single phase with a tungsten-bronze structure ($Ba_{3.99}Sm_{9.34}Ti_{18}O_{54}$, PDF#89-4356). The detailed XRD data with a $2\theta$ range of 31°~35° are presented in Fig. 2(b), which shows that the peaks shift towards higher degrees as $z$ value increases, indicating that the cell volume decreases. This demonstrates that $Al^{3+}$ with a smaller ionic radius (0.54 Å, CN = 6) successfully enters into the lattice and substitutes for $Ti^{4+}$ with a larger ionic radius (0.61 Å, CN = 6). Rietveld refinement was performed to further explore the changes of phase composition and lattice parameters with doping amount. Figure 3(a)-(c) shows the refined results of the BNT, BNT-A ($z$ = 1.25) and BNT-AN ($z$ = 1.25) ceramics as examples, respectively. The fitting results are in good agreement with experimental XRD patterns. Figure 3(d) shows that there are a few peaks that cannot be fitted in the experimental data of the BNT-A ceramics, together with $\chi^2$ rises as $z$ value

unknown secondary phase appears. In contrast, Fig. 3(e) shows that there is no secondary phase peak in the experimental data of the BNT-AN ceramics. The above-mentioned unknown secondary phase may have an impact on the microwave dielectric properties of the BNT-A ceramics.

The lattice parameters and cell volumes calculated by Rietveld refinement are shown in Fig. 4. The lattice parameters and cell volumes of the BNT-A and BNT-AN ceramics both decrease with the increase in *z* value, and basically shows the same linear decrease trend as $z \leq 1.25$. This indicates that the type of trivalent cations ($Al^{3+}$ or $Nd^{3+}$) filling the vacancies at the *A*1 sites may have less influence on the lattice parameters in the doping process of the BNT ceramics. When $z \geq 1.25$, the lattice parameters and cell volumes of the BNT-AN ceramics continuously show a linear decreasing trend, while the decreasing trend of those of the BNT-A ceramics deviates from linearity. Combining with Fig. 3(d)(e), it can be demonstrated that such a deviation is caused by the secondary phase in the BNT-A ceramics. Therefore, the BNT-A ceramics cannot form a complete solid solution phase when more $Al^{3+}$ ions are added, while the BNT-AN ceramics can form a continuous solid solution in the range of $0 \leq z \leq 2$. The detailed results of the structural parameters and reliability factors obtained by Rietveld refinement are shown in Table S1 and Table S2.

Figure 5 presents the relative densities and microwave dielectric properties of the BNT-A and BNT-AN ceramics. According to Fig. 5(a), the relative densities of almost all ceramic samples have reached higher than 97%, indicating the ceramics are all well densified. When $z \geq 1$, the relative densities of the BNT-AN ceramics is lower than those of BNT-A ceramics with the same doping amount. In addition, the sintering temperature of the BNT-AN ceramics is higher with large *z* values as illustrated in SEM results. Therefore, the BNT-AN ceramics are more difficult to be well-sintered than the BNT-A ceramics. Figure 5(b)(d) show that the $\varepsilon_r$ and $\tau_f$ values of the ceramics decrease in a similar trend with the increase in *z* value, which is consistent with the reports of low-valence cations doping at the *B* sites in BLT system [28–36]. According to Shannon's rule [41], $\varepsilon_r$ is related to the ionic polarizability ($\alpha_D$) and the molecular volume ($V_m$):

$$\alpha_{\mathrm{D}} = \frac{V_{\mathrm{m}}\left(\epsilon_{\mathrm{rc}}-1\right)}{\mathrm{b}\left(\epsilon_{\mathrm{rc}}+2\right)} \#(1)$$

where $\varepsilon_{rc}$ is the corrected dielectric constant and b is a constant equal to 4π/3. According to Eq. (1), $\varepsilon_{rc}$ increases when $\alpha_D$ increases or $V_m$ decreases. Although the cell volume of the ceramics decreases slightly when *z* value increases as shown in Fig. 4, the decrease in $\alpha_D$ [$\alpha(Al^{3+}) < \alpha(Ti^{4+})$] may mainly dominate the decrease in $\varepsilon_r$. Reaney et al. [6] reported that $\tau_f$ is usually determined by $\varepsilon_r$, and the change trends of $\varepsilon_r$ and $\tau_f$ are often similar in the same ceramic system. When $z \geq 1.25$, the decrease in $\varepsilon_r$ of the BNT-A ceramics slows down, and may be related to the small amount of secondary phase, consistent with the previous results of Al-doping in BLT system [35]. Figure 5(c) shows that when $z \leq 1.5$, the $Q \times f$ values of the ceramics significantly increase as *z* value increases, which may be related to the decline in the activity of $V_O^{\bullet\bullet}$ illustrated by TSDC technique in our past research [35]. As $z \geq 1.5$, the continuous doping makes the $Q\times f$ values of the ceramics decrease slightly. The decrease in the $Q\times f$ values of the BNT-A ceramics may be affected by the secondary phase, and that of BNT-AN ceramics may be related to the decline of densification. BNT-AN ceramics with $z = 1.25$ have reached excellent microwave dielectric properties: $\varepsilon_r = 72.2$, $Q\times f = 16480$ GHz, and $\tau_f = +14.3$ ppm/℃.

It is noticed from Fig. 5(b)(c) that when $z \le 1.5$, the $\varepsilon_r$ and $Q\times f$ values of the BNT-AN ceramics are both higher than those of the BNT-A ceramics with the same doping amount, indicating that Al/Nd co-doping may be a superior strategy for substitution in the BNT ceramics. The comparison of the $\varepsilon_r$ and $Q\times f$ values of these ceramics is visually presented in Fig. 6. This important difference in microwave dielectric properties may be related to factors such as the composition, structure and defects of the ceramics. The trivalent cations filling the vacancies at the $A1$ sites have different polarizabilities [$\alpha(Al^{3+}) < \alpha(Nd^{3+})$], which results in higher $\varepsilon_r$ values of BNT-AN ceramics according to Shannon's rule [41]. As for the $Q\times f$ values, the determinants may become more complicated: in addition to the secondary phase and porosity that have been discussed, the defects and stability of crystal lattice may also play an important role [6, 42]. Bond length, bond valence and bond energy are important factors that reflect the stability of crystal lattice, and have been used to explore the relationship between the structure and properties of microwave dielectric properties [43–45]. However, according to the results of Rietveld refinement, the variation of the average bond length of the ceramics related to $z$ value is less than 0.01 Å, which is roughly equivalent to the uncertainty of Rietveld refinement method (~ 0.006 Å). The average bond length of $A1$-O is shown in Fig. S1 as an example. These data could hardly be used for further analysis. Therefore, Raman spectroscopy and TSDC technique are performed to further explore the relationship among the crystal structure, defects and $Q\times f$ values of the ceramics.

Raman spectroscopy can reflect the lattice vibration information of materials. The polarization mechanism of dielectrics in the microwave frequency band is mainly ion displacement polarization [46], which is closely related to the vibration of ions in the crystal lattice. Therefore, Raman spectroscopy is a powerful tool for studying the relationship between the structure and properties of microwave dielectric ceramics [20, 32, 47–53]. The space group of the BLT superlattice with tungsten-bronze structure is Pbnm (No. 62), and there are 24 Raman active vibration modes: $7A_g + 7B_g + 5B_{2g} + 5B_{3g}$ [54]. The Raman spectra results of the BNT-A and BNT-AN ceramics are presented in Fig. 7. A total of 17 Raman vibration modes were observed in the experimental data. As the Raman spectra of the BLT system are excessively complex, previous studies had different opinions on the identification of Raman modes. Nevertheless, most studies considered that the Raman vibration modes in the region of 100 ~ 200 $cm^{-1}$ correspond to $A$-site cations translation. The vibration modes in the regions of 200 ~ 400 $cm^{-1}$ and 400 ~ 600 $cm^{-1}$ were attributed to the rotation and the internal vibration of the $TiO_6$ octahedra, respectively. The mode at 757 $cm^{-1}$ might correspond to the second order scatter [20, 32, 51–53]. Limited by the test conditions, vibration modes between 50 $cm^{-1}$ and 100 $cm^{-1}$ in BLT system have not been reported yet. Previous studies on perovskite systems such as $SmAlO_3$, $NdNiO_3$, $LaGaO_3$ and $BaCeO_3$, which also have the space group symmetry Pbnm, reported Raman modes in the region of 50 ~ 100 $cm^{-1}$ and identified all those

Loading [MathJax]/jax/output/CommonHTML/jax.js

modes as *A*-site cations translation [54–59]. Therefore, in the BNT-A and BNT-AN systems, the vibration modes between 50 $\text{cm}^{-1}$ and 100 $\text{cm}^{-1}$ are identified as *A*-site cations translation as well as the vibration modes between 100 $\text{cm}^{-1}$ and 200 $\text{cm}^{-1}$. It is reported that the mode at 234 $\text{cm}^{-1}$ was considered as the tilting vibration of the $TiO_6$ octahedra when the *A* sites are occupied by $Ba^{2+}$ [48, 54]. The doping methods in the present work have not made any changes to the $Ba^{2+}$ cations occupying the *A*2 sites, so it can be considered that this mode does not change significantly. In order to compare the intensities of the Raman modes, the relative intensities of the Raman spectra in Fig. 7 were obtained by normalizing the experimental intensities based on the peak values of the Raman mode at 234 $\text{cm}^{-1}$.

As shown in Fig. 7, with the increase in *z* value, most of the Raman modes present a blue-shift, which indicates that the cell volume decreases [20, 32, 46, 49, 52, 53, 60], consistent with the XRD results. The relative intensities of the vibration modes in the region of 300 ~ 400 $\text{cm}^{-1}$ increase slightly as *z* value increases, implying that the tilting vibration of the $TiO_6$ octahedra becomes stronger, and the decline of $\tau_f$ is related to this phenomenon [48, 51, 53]. The more obvious changes appear in the vibration modes between 50 $\text{cm}^{-1}$ and 200 $\text{cm}^{-1}$, which are identified as *A*-site cations translation. As *z* value increases, the relative intensities of these Raman modes are significantly reduced, where the variation of relative intensities of the Raman modes at 80 $\text{cm}^{-1}$ and 94 $\text{cm}^{-1}$ is shown in Fig. 8 as an example. It represents that the *A*-site cations translation is weakened, indicating that the binding force towards the *A*-site cations is strengthened, and accordingly the contribution to the microwave dielectric loss is reduced and the $Q \times f$ values increase. Comparing the Raman spectra of BNT-A and BNT-AN ceramics with the same *z* value, it is found that the relative intensities of the Raman modes at 80 $\text{cm}^{-1}$ and 94 $\text{cm}^{-1}$ of the BNT-AN ceramics are lower than those of the BNT-A ceramics, as shown in Fig. 8. It is implied that the strength of the A-site cation vibration in the BNT-AN ceramics is weaker, so the contribution to the microwave dielectric loss is lower and the $Q \times f$ values is higher. Briefly, the relationship between the $Q \times f$ values and the strength of the A-site cation vibration in the BNT-A and BNT-AN systems has been established through Raman spectroscopy.

TSDC technique can provide valuable information on the types and concentrations of defects in dielectrics, and has been widely used to explore the dielectric response mechanism of ceramics [35, 61–68]. Liu et al. [61] firstly reported the method for determining the types of defects in inorganic dielectrics through the changes in peak position ($T_m$, the temperature at which the absolute value of current density is maximized) and peak intensity ($J_m$, the maximum of the absolute value of current density) of the TSDC curves with various polarization conditions ($T_p$ and $E_p$), and Zhang et al. [66] applied this method to microwave dielectric ceramics for the first time. Figure 9 shows the TSDC curves of the BNT, BNT-A ($z$ = 1.25) and BNT-AN ($z$ = 1.25) ceramics. The curves of all samples show three or four TSDC peaks, indicating that there are at least three or four defect relaxation mechanisms, respectively. In the range of 50 °C < $T_m$ < 150 °C, there is a weak peak (referred to as peaks $A_1$, $A_2$ and $A_3$) in each figure. And peaks similar to each other (referred to as peaks $B_1$, $B_2$ and $B_3$) are displayed in the range of 160 °C < $T_m$ < 200 °C. The TSDC curves of different samples are quite different in the high temperature section above 200

Loading [MathJax]/jax/output/CommonHTML/jax.js

°C. The curves of undoped sample exhibit a very strong peak (referred to as peak $D_1$), and its $T_m$ values have exceeded the test range. The curves of two doped samples both show peaks with similar changes (referred to as peaks $C_2$ and $C_3$) at around 240 °C. The TSDC curves of the BNT-A ($z = 1.25$) ceramics also show a weak peak (referred to as peak $D_2$) with $T_m > 280$ °C.

The $T_m$ and $J_m$ of peaks $A_1$ and $A_3$ both increase with an increase in $E_p$, indicating that these peaks are likely related to the relaxation of $V_O^{\bullet\bullet}$. As $E_p$ increases, the $J_m$ of peak $A_2$ increases while the $T_m$ decreases, indicating that peak $A_2$ may be related to the relaxation of trapped charges. Using the initial rise method [66, 69], the activation energies of peaks $A_1$, $A_2$ and $A_3$ are calculated as 0.43 ~ 0.50 eV, 0.14 ~ 0.17 eV and 0.24 ~ 0.36 eV, respectively. Based on previous results [35, 64, 65], the activation energies of peaks $A_1$ and $A_3$ are close to those of the in-grain $V_O^{\bullet\bullet}$, and it can be inferred that these peaks are related to the relaxation of the in-grain $V_O^{\bullet\bullet}$. The $T_m$ and activation energy of peak $A_2$ are similar to those of peaks $A_1$ and $A_3$, and it is speculated that peak $A_2$ may correspond to trap charges associated with the in-grain $V_O^{\bullet\bullet}$. Peaks $B_1$, $B_2$, $B_3$, $C_2$ and $C_3$ have $T_m$ values which basically unchanged with polarization conditions, while their $J_m$ values increase with an increase in $E_p$, indicating that they may be related to the relaxation of defect dipoles. The calculated activation energies of peaks $B_1$, $B_2$ and $B_3$ are 0.58 ~ 0.80 eV, 0.64 ~ 0.75 eV and 0.59 ~ 0.75 eV, respectively. According to the results from previous studies [35, 63, 70], it can be inferred that peak B is related to the relaxation of the $\mathrm{Ti}_{\mathrm{Ti}}^{'} - V_O^{\bullet\bullet}$ defect dipoles. Although the activation energies of peaks $C_2$ and $C_3$ are difficult to calculate by the initial rise method, the type of defects related to peak C could be determined by the defect reactions in the doping process, considering that peak C appears only after doping. During the substitution process of $Al^{3+}$ for $Ti^{4+}$ at the $B$ sites, $\mathrm{Al}_{\mathrm{Ti}}^{'}$ point defects are formed. Meanwhile, excess trivalent cations ($Al^{3+}$ or $Nd^{3+}$) were added to fill the vacancies at the $A1$ sites, forming $\mathrm{Al}_{A1}^{\bullet\bullet\bullet}$ or $\mathrm{Nd}_{A1}^{\bullet\bullet\bullet}$ point defects. Thus the condition of charge balance could be ensured, without ion valence changing or $V_O^{\bullet\bullet}$ producing. Therefore, peak $C_2$ and $C_3$ are considered as the relaxation peaks of the $\mathrm{Al}_{\mathrm{Ti}}^{'} - \mathrm{Al}_{A1}^{\bullet\bullet\bullet}$ and $\mathrm{Al}_{\mathrm{Ti}}^{'} - \mathrm{Nd}_{A1}^{\bullet\bullet\bullet}$ defect dipoles, respectively. As for peak $D_1$, the current density rises slower when $E_p$ is higher, indicating that it will reach a peak value at a higher temperature with higher $E_p$, which signifies that peak $D_1$ may be related to the relaxation of $V_O^{\bullet\bullet}$. The calculated activation energy of peak $D_1$ is 0.98 ~ 1.19 eV, similar to that of the across-grain-boundary $V_O^{\bullet\bullet}$ (1.1 eV) [35, 62]. It is implied that peak $D_1$ is likely related to the relaxation of the across-grain-boundary $V_O^{\bullet\bullet}$. Since the position of peak $D_2$ is similar to peak $D_1$, it is speculated that the relaxation mechanisms of the two are the same, so that it can be considered that peak $D_2$ is also related to the relaxation of the across-grain-boundary $V_O^{\bullet\bullet}$.

TSDC peaks with higher $J_m$ imply a higher concentration of the corresponding defects [68, 71]. Comparing the TSDC curves of the three ceramic samples, the BNT ceramics with peak $D_1$ in Fig. 9(a) e across-grain-boundary $V_O^{\bullet\bullet}$, while the BNT-A ($z = 1.25$)

ceramics with peak $D_2$ in Fig. 9(b) show only a small amount of across-grain-boundary $V_O^{\bullet\bullet}$, and the BNT-AN ($z$ = 1.25) ceramics show no peaks corresponding to across-grain-boundary $V_O^{\bullet\bullet}$ in Fig. 9(c). It is generally believed that oxygen vacancies could cause the extrinsic loss of dielectric ceramics and affect the $Q \times f$ values at microwave frequency bands [6]. The TSDC results in the present work are consistent with it. It is noticed that each $O^{2-}$ in the crystal lattice is adjacent to several *A*-site cations in BLT system. Associating the results of TSDC with the aforementioned Raman spectroscopy of the BNT-A and BNT-AN ceramics, it can be found that with the strengthening of binding force between the *A*-site cations and $O^{2-}$, the formation of $V_O^{\bullet\bullet}$ becomes difficult, indicating that the results of TSDC and Raman spectroscopy are consistent. It is demonstrated for the first time that in the structural and defect modulation of the BNT ceramics, the formation of $V_O^{\bullet\bullet}$ in the crystal lattice is closely related to the strength of the *A*-site cation vibration, and $V_O^{\bullet\bullet}$ affects the lattice vibration then affects the microwave dielectric loss.

# 4 Conclusions

The Al-doped and Al/Nd co-doped BNT ceramics are prepared through the solid state processing. The microwave dielectric properties of the BNT-A and BNT-AN ceramics are compared, and the relationship among the composition, structure, defects and microwave dielectric properties of the ceramics was explored through Rietveld refinement, Raman spectroscopy and TSDC technique. As the doping amount increases, the $\varepsilon_r$ and $\tau_f$ values of the ceramics decrease, and the $Q \times f$ values first increase and then slightly decrease. The $\varepsilon_r$ and $Q \times f$ values of BNT-AN ceramics are both higher than those of BNT-A ceramics, indicating that Al/Nd co-doping is a novel and superior doping method that maintains the condition of charge balance. The results of Rietveld refinement show that there is a small amount of unknown secondary phase in the BNT-A ceramics, and the relative density data show that the BNT-AN ceramics are more difficult to densify, which may result in the deterioration of microwave dielectric performance when $z \geq 1.5$. Raman spectroscopy and TSDC measurement together show that the $Q \times f$ values of the BNT-A and BNT-AN ceramics are closely related to the strength of the *A*-site cation vibration and the concentration of $V_O^{\bullet\bullet}$. With the strengthening of binding force between the *A*-site cations and $O^{2-}$, the contribution of the *A*-site cations to the microwave dielectric loss reduces and the $Q \times f$ values decrease, together with that the formation of $V_O^{\bullet\bullet}$ becomes difficult. It is also proved that in microwave frequency bands, oxygen vacancies affect the dielectric loss by affecting the lattice vibration. Microwave dielectric ceramics with excellent performance in the field of medium/high $\varepsilon_r$ were obtained by the structural and defect modulation strategy: $\varepsilon_r = 72.2$, $Q \times f = 16480$ GHz, and $\tau_f = +14.3$ ppm/℃, which could have outstanding application prospects in the 5G technology.

# Declarations

## Acknowledgements

This work was supported by the National Key Research and Development Program of China (Grant No. 2017YFB0406301), Key-Area Research and Development Program of Guangdong Province (Grant No. 2020B010176001), and the National Natural Science Foundation of China (Grant No.51872160).

### Electronic Supplementary Material

Supplementary material (add a brief description) is available in the online version of this article.

## References

1. Hill MD, Cruickshank DB, MacFarlane IA. Perspective on ceramic materials for 5G wireless communication systems. *Appl Phys Lett* 2020, **118**: 120501.
2. Jin DH, Hu CC, Liu B. Improved sinterability and temperature stability in $Zn^{2+}/Ti^{4+}$-co-substituted $CaAl_2O_4$ ceramics and their 5G antenna applications. *J Mater Sci: Mater Electron* 2021, **32**: 18205-18211.
3. Zhang L, Zhang J, Yue Z, et al. Thermally stable polymer-ceramic composites for microwave antenna applications. *J Adv Ceram* 2016, **5**: 269-276.
4. Medeiros JLG. Microstrip fractal patch antennas using high permittivity ceramic substrate. In *Proc IEEE Antennas and Propagation Society Int Symp (APSURSI)*. Chicago, 2012: 1-2.
5. Rhbanou A, Fadl AE, Jebbor N, et al. New design of miniature C-band substrate integrated waveguide bandpass filters using ceramic material. *FME Trans*, 2021, **49**: 103-112.
6. Reaney IM. Microwave dielectric ceramics for resonators and filters in mobile phone networks. *J Am Ceram Soc* 2006, **89**: 2063-2072.
7. Cohn SB. Microwave bandpass filters containing high-$Q$ dielectric resonators. *IEEE Trans Microw Theory Tech*, 1968, **16**: 218-227.
8. Zhao E, Hao J, Xue X, et al. Rutile $TiO_2$ microwave dielectric ceramics prepared via cold sintering assisted two step sintering. *J Eur Ceram Soc*, 2021, **41**: 3459-3465.
9. Ohsato H, Ohhashi T, Nishigaki, et al. Formation of solid solutions of new tungsten bronze-type microwave dielectric compounds $Ba_{6-3x}R_{8+2x}Ti_{18}O_{54}$ ($R$ = Nd and Sm, $0 \le x \le 1$). *Jpn J Appl Phys*, 1993, **32**: 4323-4326.
10. Ohsato H. Science of tungstenbronze-type like $Ba_{6-3x}R_{8+2x}Ti_{18}O_{54}$ ($R$ = rare earth) microwave dielectric solid solutions. *J Eur Ceram Soc*, 2001, **21**: 2703-2711.
11. Ezaki K, Baba Y, Takahashi H, et al. Microwave dielectric properties of $CaO$-$Li_2O$-$Ln_2O_3$-$TiO_2$ ceramics. *Jpn J Appl Phys*, 1993, **32**: 4319-4322.
12. Zhou C, Chen G, Cen Z, et al. Structure and microwave dielectric characteristics of lithium-excess $Ca_{0.6}Nd_{0.8/3}TiO_3/(Li_{0.5}Nd_{0.5})TiO_3$ ceramics. *Mater Res Bull*, 2013, **48**: 4924-4929.
13. Yoshida M, Hara N, Takada T, et al. Structure and dielectric properties of $(Ca_{1-x}Nd_{2x/3})TiO_3$. *Jpn J Appl Phys* 1997, **36**: 6818-6823.

14. Kim WS, Kim ES, Yoon KH. Effects of $Sm^{3+}$ substitution on dielectric properties of $Ca_{1-x}Sm_{2x/3}TiO_3$ ceramics at microwave frequencies. *J Am Ceram Soc*, 1999, **82**: 2111-2115.

15. Huang C-L, Tsai J-T, Chen Y-B. Dielectric properties of $(1-y)Ca_{1-x}La_{2x/3}TiO_3$-$y(Li,Nd)_{1/2}TiO_3$ ceramic system at microwave frequency. *Mater Res Bull*, 2001, **36**: 547-556.

16. Kato J, Kagata H, Nishimoto K. Dielectric properties of $(PbCa)(MeNb)O_3$ at microwave frequencies. *Jpn J Appl Phys* 1992, **31**: 3144-3147.

17. Kucheiko S, Choi J-W, Kim H-J, et al. Microwave characteristics of $(Pb,Ca)(Fe,Nb,Sn)O_3$ dielectric materials. *J Am Ceram Soc* 1997, **80**: 2937-2940.

18. Huang X, Liu X, Liu F, et al. Microstructures and microwave dielectric properties of $(Ba_{1-x}Sr_x)_4(Sm_{0.4}Nd_{0.6})_{28/3}Ti_{18}O_{54}$ solid solutions. *J Adv Ceram* 2017, **6**: 50-58.

19. He T, Lv C, Li W, et al. The dielectric constant of $Ba_{6-3x}(Sm_{1-y}Nd_y)_{8+2x}Ti_{18}O_{54}$ ($x$ = 2/3) ceramics for microwave communication by linear regression analysis. *Materials* 2020, **13**: 5733.

20. Wang G, Fu Q, Guo P, et al. Crystal structure, spectra analysis and dielectric characteristics of $Ba_4M_{28/3}Ti_{18}O_{54}$ (M = La, Pr, Nd, and Sm) microwave ceramics. *Ceram Int* 2021, **47**: 1750-1757.

21. Chen Y, Guo W, Luo Y, et al. Microwave and terahertz properties of porous $Ba_4(Sm,Nd,Bi)_{28/3}Ti_{18}O_{54}$ ceramics obtained by sacrificial template method. *J Am Ceram Soc* 2021, **00**: 1-10. https://doi.org/10.1111/jace.17940

22. Hsiang H-I, Chen C-C, Yang S-Y. Microwave dielectric properties of $Ca_{0.7}Nd_{0.2}TiO_3$ ceramic-filled CaO-$B_2O_3$-$SiO_2$ glass for LTCC applications. *J Adv Ceram* 2019, **8**: 345-351.

23. Lin S-H, Lin Z-Q, Chen C-W. Microwave dielectric characterization of $Ca_{0.6}(La_{1-x}Y_x)_{0.2667}TiO_3$ perovskite ceramics with high positive temperature coefficient. *Ceram Int* 2021, **47**: 16828-16832.

24. Zhou D, Pang L-X, Wang D-W, et al. High permittivity and low loss microwave dielectrics suitable for 5G resonators and low temperature co-fired ceramic architecture. *J Mater Chem C* 2017, **5**, 10094-10098.

25. Ullah A, Liu H, Manan A, et al. Microwave dielectric properties of $Bi_2(Li_{0.5}Ta_{1.5})O_7$-$TiO_2$-based ceramics for 5G cellular base station resonator application. *Ceram Int* 2021, **47**: 8416-8423.

26. Peng L-X, Zhou D, Qi Z-M, et al. Structure-property relationships of low sintering temperature scheelite-structured $(1-x)BiVO_4$-$xLaNbO_4$ microwave dielectric ceramics. *J Mater Chem C* 2017, **5**: 2695-2701.

27. Pang L-X, Zhou D, Liu W-G, et al. Crystal structure and microwave dielectric behaviors of scheelite structured $(1-x)BiVO_4$-$xLa_{2/3}MoO_4$ ($0.0 \le x \le 1.0$) ceramics with ultra-low sintering temperature. *J Eur Ceram Soc* 2018, **38**: 1535-1540.

28. Chen H, Tang B, Gao A, et al. Aluminum substitution for titanium in $Ba_{3.75}Nd_{9.5}Ti_{18}O_{54}$ microwave dielectric ceramics. *J Mater Sci: Mater Electron* 2015, **26**: 405-410.

29. Tao J, Mu M, Wang X, et al. Improved microwave dielectric properties of anti-reduction [illegible] sintered in nitrogen atmosphere. *J Mater Sci: Mater Electron*

2018, **29**: 1392-1398.

30. Guo X, Tang B, Liu J, et al. Microwave dielectric properties and microstructure of $Ba_{6-3x}Nd_{8+2x}Ti_{18-y}(Cr_{1/2}Nb_{1/2})_yO_{54}$ ceramics. *J Alloy Compd* 2015, **646**: 512-516.
31. Chen H, Tang B, Duan S, et al. Microstructure and microwave dielectric properties of $Ba_{3.75}Nd_{9.5}Ti_{18-z}(Mg_{1/3}Nb_{2/3})_zO_{54}$ Ceramics. *J Electron Mater* 2015, **44**: 1081-1087.
32. Xiong Z, Tang B, Fang Z, et al. Crystal structure, Raman spectroscopy and microwave dielectric properties of $Ba_{3.75}Nd_{9.5}Ti_{18-z}(Al_{1/2}Nb_{1/2})_zO_{54}$ ceramics. *J Alloy Compd* 2017, **723**: 580-588.
33. Chen H, Xiong Z, Yuan Y, et al. Dependence of microwave dielectric properties on site substitution in $Ba_{3.75}Nd_{9.5}Ti_{18}O_{54}$ ceramic. *J Mater Sci: Mater Electron* 2016, **27**: 10951-10957.
34. Tang B, Xiang Q, Fang Z, et al. Microwave dielectric properties of $Ba_{3.75}Nd_{9.5}Ti_{18-z}Cr_{4z/3}O_{54}$ ceramics. *J Mater Sci: Mater Electron* 2018, **29**: 535-540.
35. Guo W, Zhang J, Luo Y, et al. Microwave dielectric properties and thermally stimulated depolarization of Al-doped $Ba_4(Sm,Nd)_{9.33}Ti_{18}O_{54}$ ceramics. *J Am Ceram Soc* 2019, **102**: 5494-5502.
36. Wang G, Fu Q, Shi H, et al. Novel thermally stable, high quality factor $Ba_4(Pr_{0.4}Sm_{0.6})_{28/3}Ti_{18-y}Ga_{4y/3}O_{54}$ microwave dielectric ceramics. *J Am Ceram Soc* 2020, **103**: 2520-2527.
37. Rodriguez-Carvajal J. FullProf suite 2000 (Version September 2020, Laboratoire Leon Brillouin).
38. Hakki BW, Coleman PD. A dielectric resonator method of measuring inductive capacities in the millimeter range. *IRE Trans Microwave Theory Tech* 1960, **8**: 402-410.
39. Courtney WE. Analysis and evaluation of a method of measuring the complex permittivity and permeability microwave insulators. *IEEE Trans Microwave Theory Tech* 1970, **18**: 476-485.
40. Krupka J, Derzakowski K, Riddle B, et al. A dielectric resonator for measurements of complex permittivity of low loss dielectric materials as a function of temperature. *Meas Sci Technol* 1998, **9**: 1751-1756.
41. Shannon RD. Dielectric polarizabilities of ions in oxides and fluorides. *J Appl Phys* 1993, **73**: 348-366.
42. Pei C, Tan J, Li Y, et al. Effect of Sb-site nonstoichiometry on the structure and microwave dielectric properties of $Li_3Mg_2Sb_{1-x}O_6$ ceramics. *J Adv Ceram* 2020, **9**: 588-594.
43. Xia W-S, Li L-X, Ning P-F, et al. Relationship between bond iconicity, lattice energy, and microwave dielectric properties of $Zn(Ta_{1-x}Nb_x)_2O_6$ ceramics. *J Am Ceram Soc* 2012, **95**: 2587-2592.
44. Huang F, Su H, Li Y, et al. Low-temperature sintering and microwave dielectric properties of $CaMg_{1-x}Li_{2x}Si_2O6$ ($x$ = 0-0.3) ceramics. *J Adv Ceram* 2020, **9**: 471-480.
45. Zhou X, Liu L, Sun J, et al. Effects of $(Mg_{1/3}Sb_{2/3})^{4+}$ substitution on the structure and microwave dielectric properties of $Ce_2Zr_3(MoO_4)_9$ ceramics. *J Adv Ceram* 2021, **10**: 778-789.
46. Sebastian MT. Dielectric materials for wireless communication. Elsevier, Amsterdam, 2008.

47. Chen MY, Chia CT, Lin IN, et al. Microwave properties of $Ba(Mg_{1/3}Ta_{2/3})O_3$, $Ba(Mg_{1/3}Nb_{2/3})O_3$ and $Ba(Co_{1/3}Nb_{2/3})O_3$ ceramics revealed by Raman scattering. *J Eur Ceram Soc* 2006, **26**: 1965-1968.
48. Wu SY, Li Y, Chen XM. Raman spectra of Nd/Sn cosubstituted $Ba_{6-3x}Sm_{8+2x}Ti_{18}O_{54}$ microwave dielectric ceramics. *J Appl Phys* 2004, **96**: 5683-5686.
49. Liao Q, Li L. Structural dependence of microwave dielectric properties of ixiolite structured $ZnTiNb_2O_8$ materials: crystal structure refinement and Raman spectra study. *Dalton Trans* 2012, **41**: 6963-6969.
50. Yin C, Yu Z, Shu L, et al. A low-firing melilite ceramic $Ba_2CuGe_2O_7$ and compositional modulation on microwave dielectric properties through Mg substitution. *J Adv Ceram* 2021, **10**: 108-119.
51. Wang G, Fu Q, Shi H, et al. Suppression of oxygen vacancies generation in $Ba_{6-3x}Sm_{8+2x}Ti_{18}O_{54}$ ($x$ = 2/3) microwave dielectric ceramics through Pr substitution. *Ceram Int* 2019, **45**: 22148-22155.
52. Wang G, Fu Q, Guo P, et al. *A*/*B*-site cosubstituted $Ba_4Pr_{28/3}Ti_{18}O_{54}$ microwave dielectric ceramics with temperature stable and high *Q* in a wide range. *Ceram Int* 2020, **46**: 11474-11483.
53. Xiong Z, Tang B, Yang C, et al. Correlation between structures and microwave dielectric properties of $Ba_{3.75}Nd_{9.5-x}Sm_xTi_{17.5}(Cr_{1/2}Nb_{1/2})_{0.5}O_{54}$ ceramics. *J Alloy Compd* 2018, **740**: 492-499.
54. Wu SY, Li Y, Chen XM. Raman spectra of $Ba_{6-3x}Sm_{8+2x}Ti_{18}O_{54}$ solid solution. *J Phys Chem Solids* 2003, **64**: 2365-2368.
55. Scott JF. High-temperature Raman study of samarium aluminate. *Phys Rev B* 1970, **1**: 4182-4185.
56. Zaghrioui M, Bulou A, Laffez P, et al. Raman study of metal-insulator transition in $NdNiO_3$ thin films. *J Magn Magn Mater* 2000, **211**: 238-242.
57. Sanjuán ML, Orera VM, Merino RI, et al. Raman and x-ray study of $La_{1-x}Nd_xGaO_3$ ($0 \leq x \leq 1$) perovskite solid solutions. *J Phys: Condens Matter* 1998, **10**: 11687-11702.
58. Tompsett GA, Sammes NM, Phillips RJ. Raman spectroscopy of the $LaGaO_3$ phase transition. *J Raman Spectrosc* 1999, **30**: 497-500.
59. Loridant S, Abello L, Lucazeau G. Polarized Raman spectra of single crystals of $BaCeO_3$. *J Raman Spectrosc* 1997, **28**: 283-288.
60. Wu M, Zhang Y, Xiang M. Synthesis, characterization and dielectric properties of a novel temperature stable $(1-x)CoTiNb_2O_8-xZnNb_2O_6$ ceramic. *J Adv Ceram* 2019, **8**: 228-237.
61. Liu W, Randall CA. Thermally stimulated relaxation in Fe-doped $SrTiO_3$ systems: I. single crystals. *J Am Ceram Soc* 2008, **91**: 3245-3250.
62. Yoon S-H, Randall CA, Hur K-H. Correlation between resistance degradation and thermally stimulated depolarization current in acceptor (Mg)-doped $BaTiO_3$ submicrometer fine-grain ceramics. *J Am Ceram Soc* 2010, **93**: 1950-1956.
63. Lee H, Kim JR, Lanagan MJ, et al. High-energy density dielectrics and capacitors for elevated temperatures: $Ca(Zr,Ti)O_3$. *J Am Ceram Soc* 2013, **96**: 1209-1213.

64. Zhang X, Zhang Y, Zhang J, et al. Microwave dielectric properties and thermally stimulated depolarization currents study of (1-$x$)$Ba_{0.6}Sr_{0.4}La_4Ti_4O_{15}$-$x$$TiO_2$ ceramics. *J Am Ceram Soc* 2014, **97**: 3170-3176.
65. Zhang X, Zhang J, Xie Z, et al. Structure, microwave dielectric properties and thermally stimulated depolarization currents of (1-$x$)$Ba_{0.6}Sr_{0.4}La_4Ti_4O_{15}$-$x$$Ba_5Nb_4O_{15}$ solid solutions. *J Am Ceram Soc* 2015, **98**: 1245-1252.
66. Zhang J, Zhou Y, Peng B, et al. Microwave dielectric properties and thermally stimulated depolarization currents of $MgF_2$-doped diopside ceramics. *J Am Ceram Soc* 2014, **97**: 3537-3543.
67. Zhang J, Yue Z, Luo Y, et al. Understanding the thermally stimulated relaxation and defect behavior of Ti-containing microwave dielectrics: a case study of $BaTi_4O_9$. *Mater Des* 2017, **130**: 479-487.
68. Luo Y, Zhang J, Yue Z, et al. Improvement in microwave dielectric properties of $Sr_2TiO_4$ ceramics through post-annealing treatment. *J Electroceram* 2018, **41**: 67-72.
69. Hino T. Thermally stimulated characteristics in solid dielectrics. *IEEE Trans Electr Insul* 1980, **15**: 301-311.
70. Lee S-J, Kang K-Y, Han S-K. Low-frequency dielectric relaxation of $BaTiO_3$ thin-film capacitors. *Appl Phys Lett* 1999, **75**: 1784-1786.
71. Bräunlich P. Topics in Applied Physics: Thermally Stimulated Relaxation in Solids. Berlin, Heidelberg (DE): Springer, 1979, **37**.

## Figures

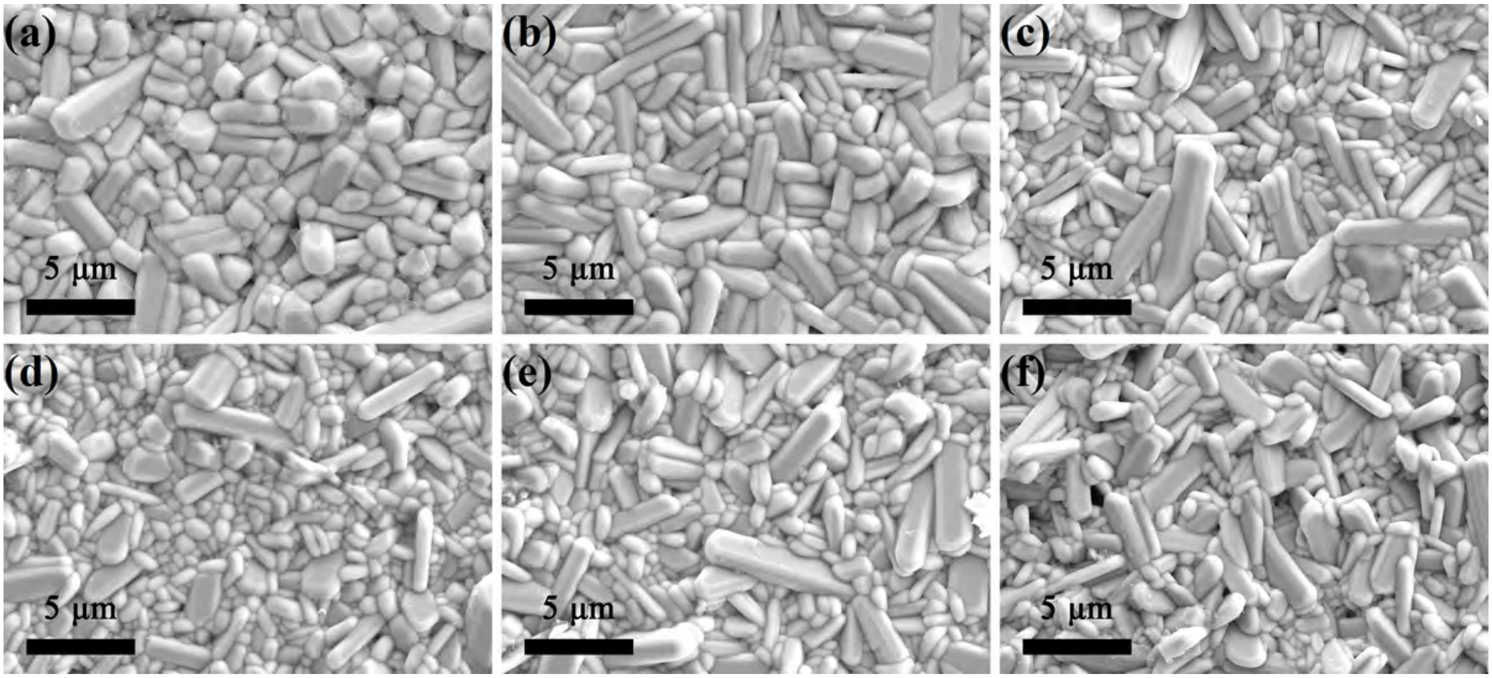

Figure 1

Loading [MathJax]/jax/output/CommonHTML/jax.js

SEM photographs of the BNT, BNT-A and BNT-AN ceramics: (a) BNT, sintered at 1400 °C; (b) BNT-A, z = 1.25, sintered at 1400 °C; (c) BNT-A, z = 2, sintered at 1400 °C; (d) BNT-AN, z = 1.25, sintered at 1400 °C; (e) BNT-AN, z = 1.25, sintered at 1500 °C; (f) BNT-A, z = 2, sintered at 1550 °C;

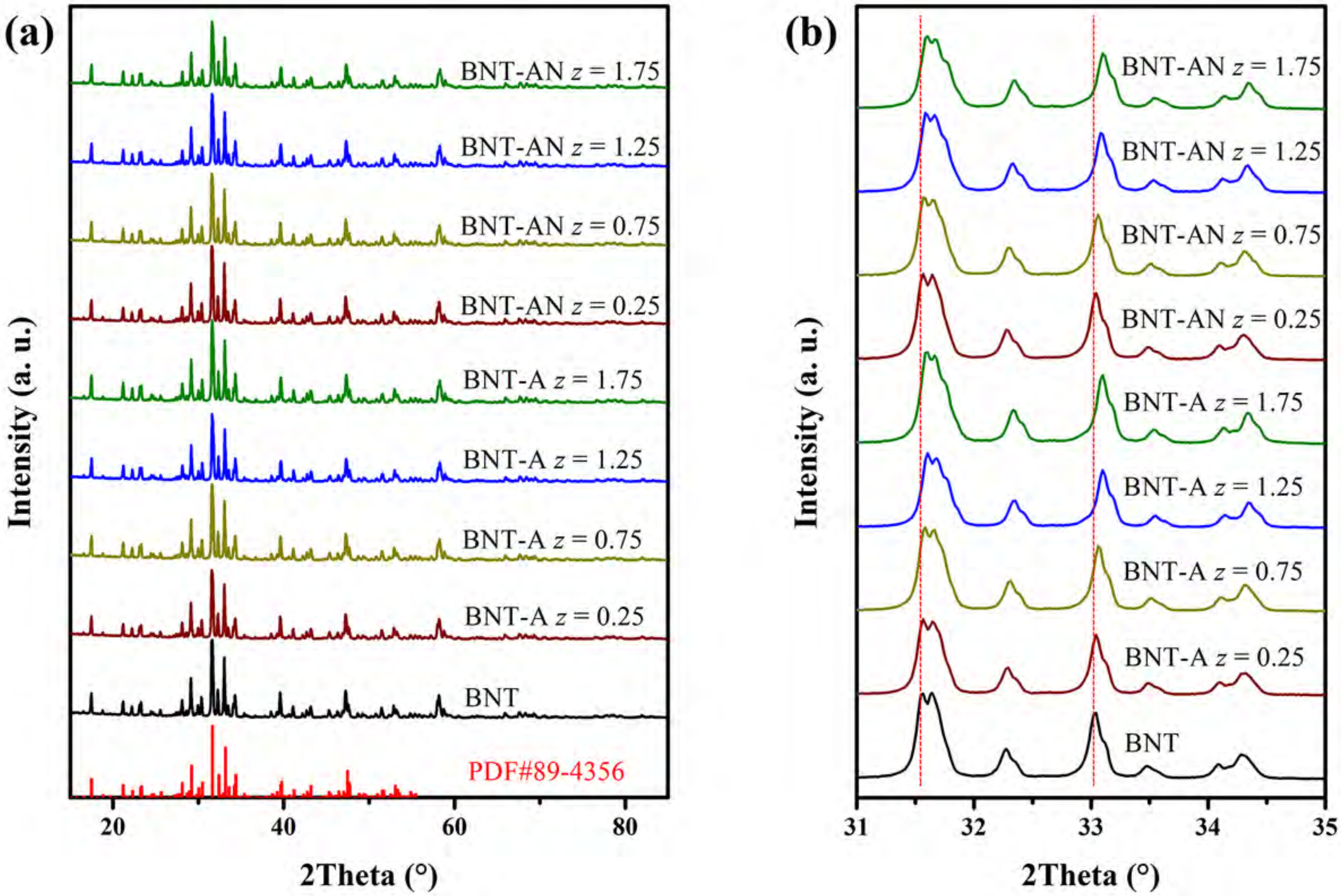

**Figure 2**

(a) XRD patterns of the BNT, BNT-A and BNT-AN ceramics (z = 0, 0.25, 0.75, 1.25, 1.75); (b) XRD peaks shift in the range of 31° ≤ 2θ ≤ 35°.

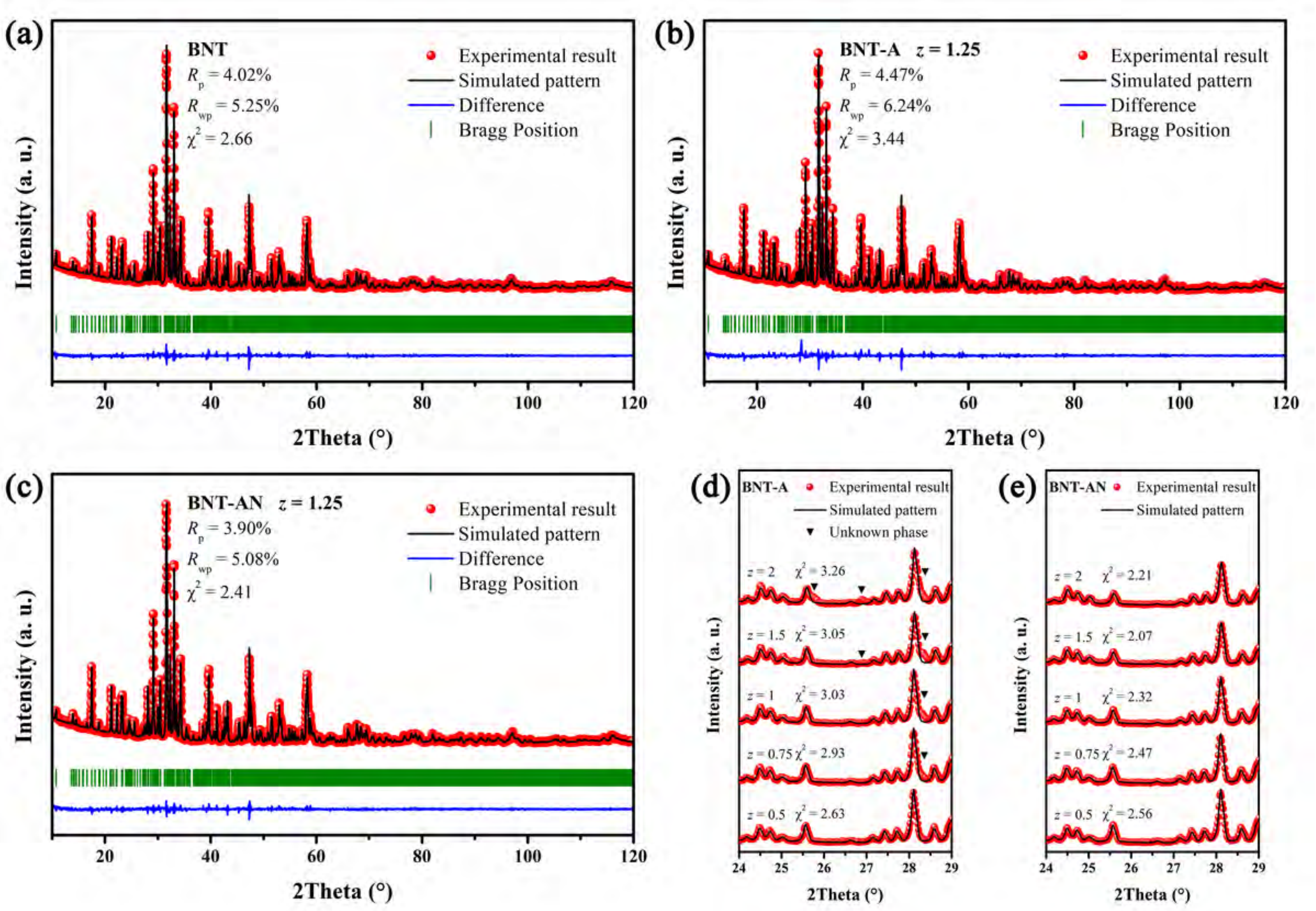

**Figure 3**

The Rietveld refinement results of (a) the BNT ceramics, (b) the BNT-A (z = 1.25) ceramics, and (c) the BNT-AN (z = 1.25) ceramics; the detailed Rietveld refinements of (d) the BNT-A (0.5 ≤ z ≤ 2) ceramics and (e) the BNT-AN (0.5 ≤ z ≤ 2) ceramics.

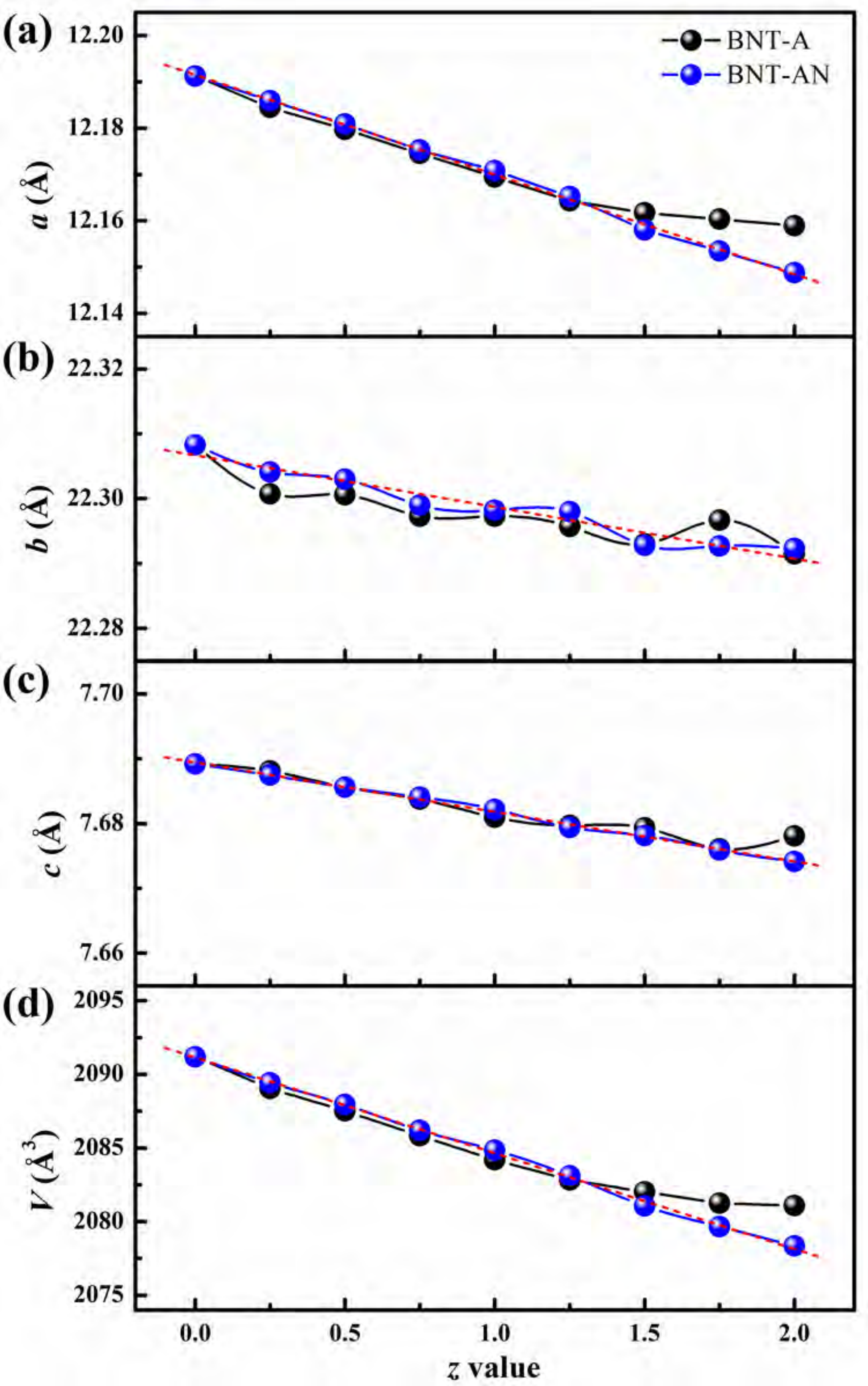

## Figure 4

The lattice parameters (a) a, (b) b, (c) c, and (d) the cell volume of the BNT-A and BNT-AN ($0 \leq z \leq 2$) ceramics.

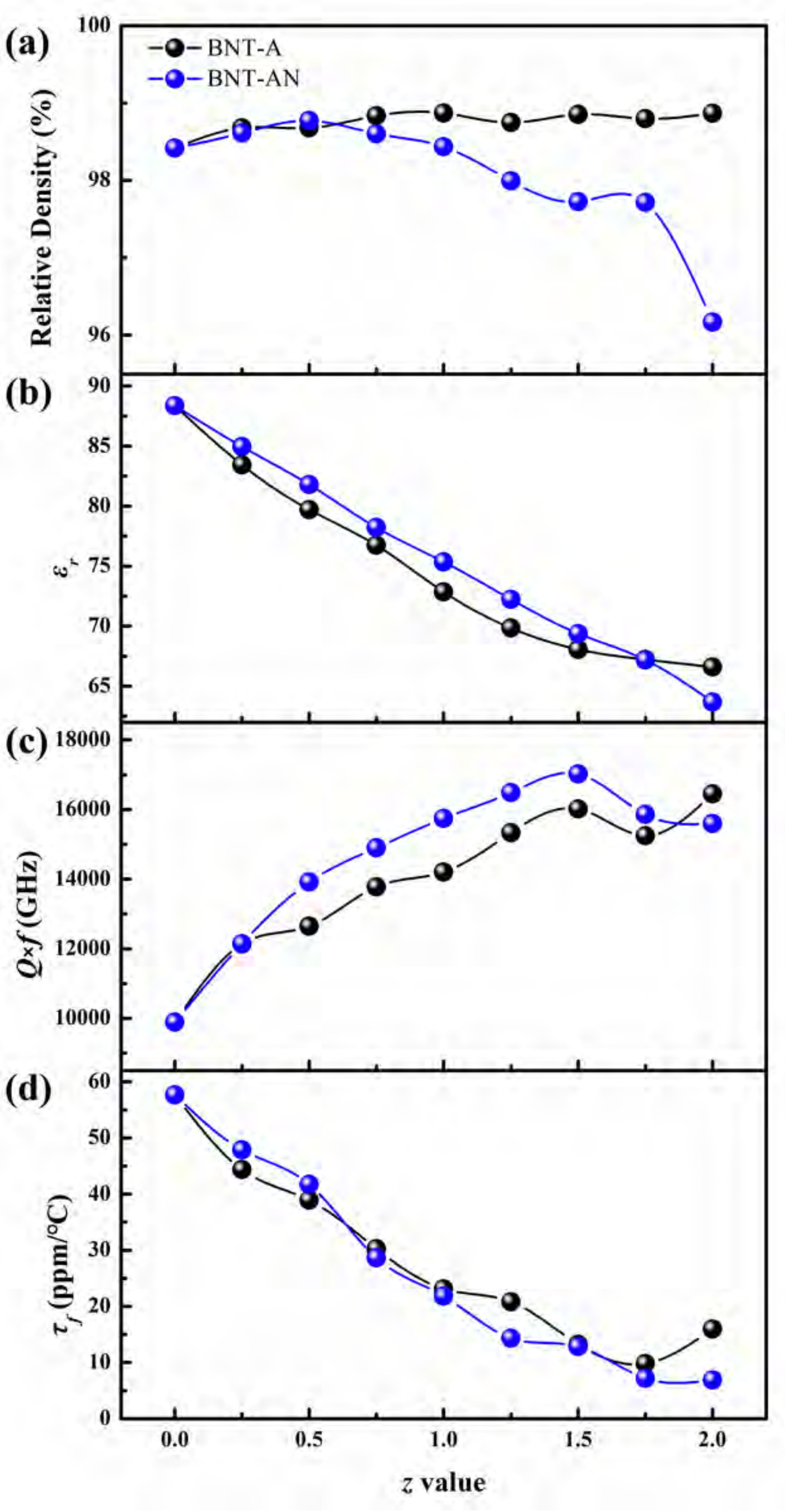

**Figure 5**

(a) Relative densities, (b) εr values, (c) Q×f values and (d) τf values of the BNT-A and BNT-AN (0 ≤ z ≤ 2) ceramics.

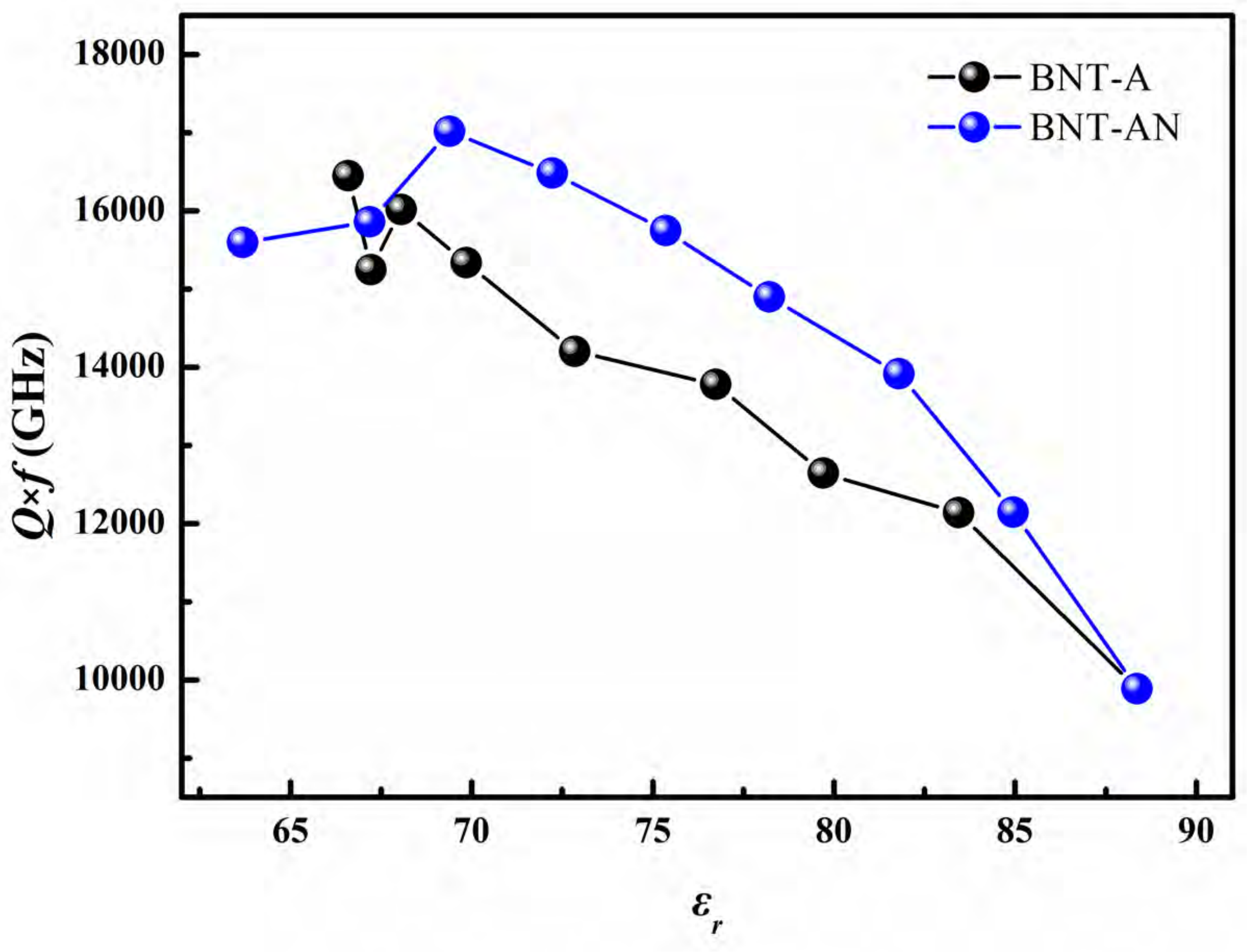

**Figure 6**

The εr and Q×f values of the BNT-A and BNT-AN (0 ≤ z ≤ 2) ceramics.

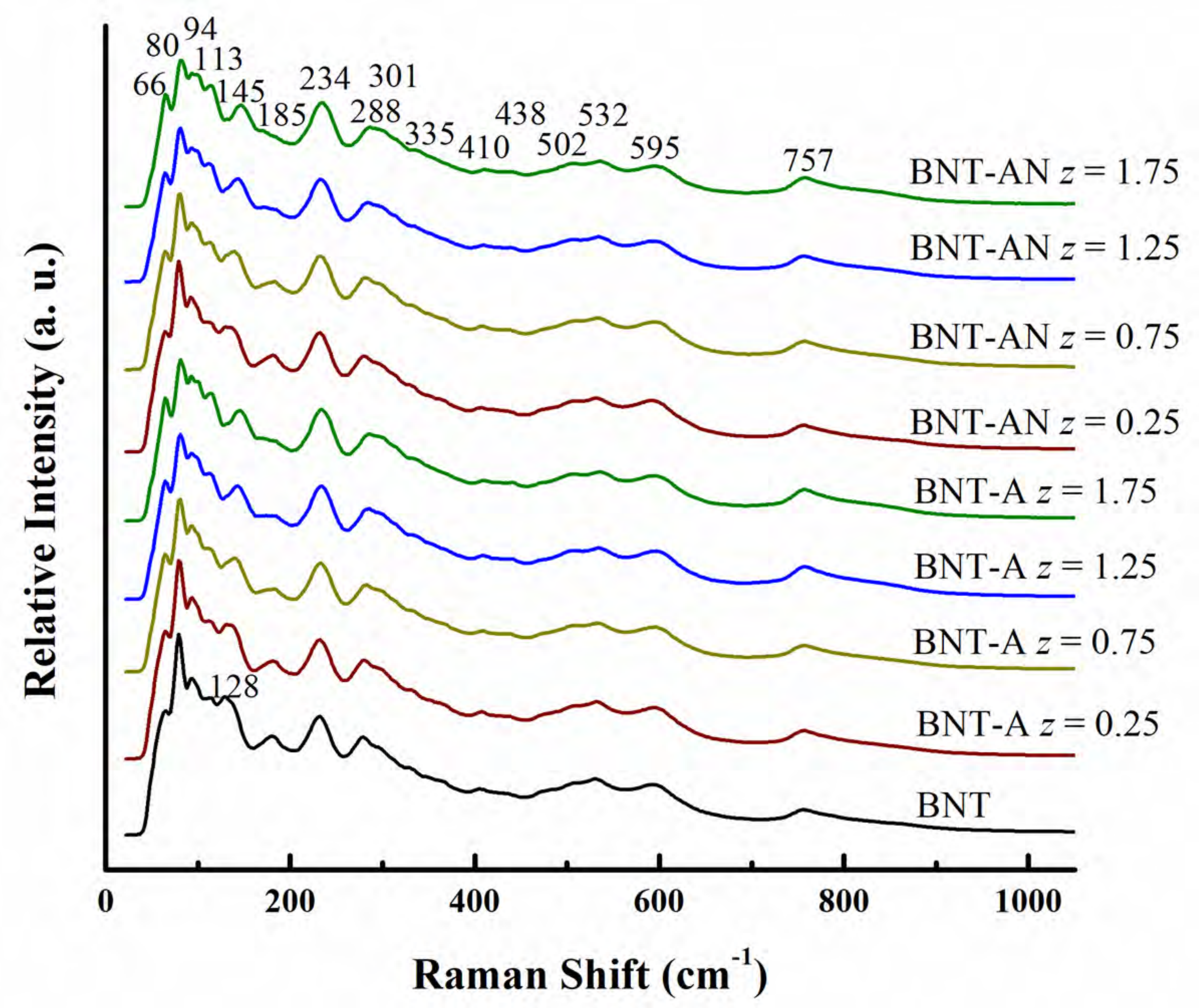

**Figure 7**

Raman spectra of the BNT-A and BNT-AN (z = 0, 0.25, 0.75, 1.25, 1.75) ceramics.

Loading [MathJax]/jax/output/CommonHTML/jax.js

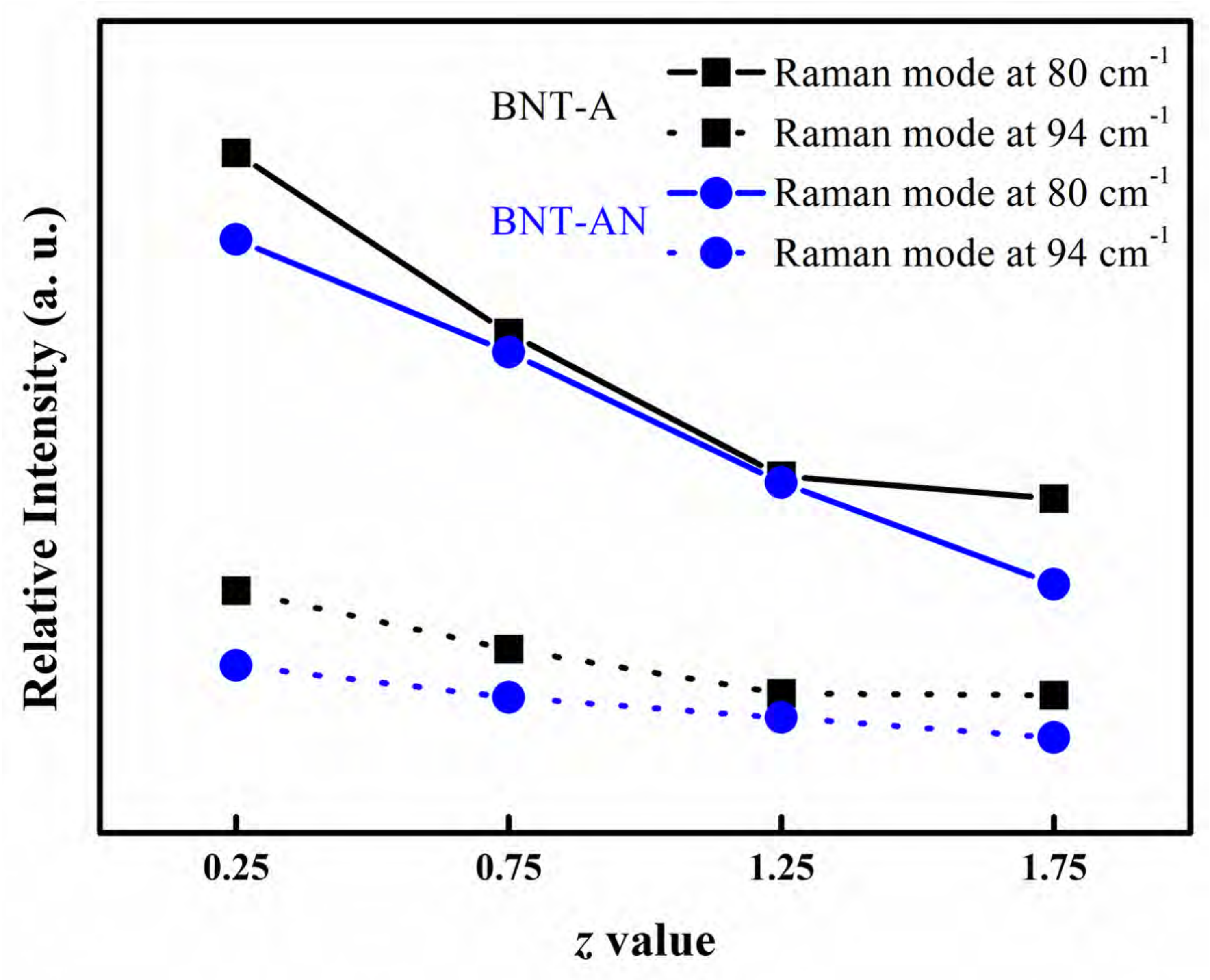

**Figure 8**

The relative intensities of Raman modes at 80 cm-1 and 94 cm-1 of the BNT-A and BNT-AN (z = 0.25, 0.75, 1.25, 1.75) ceramics.

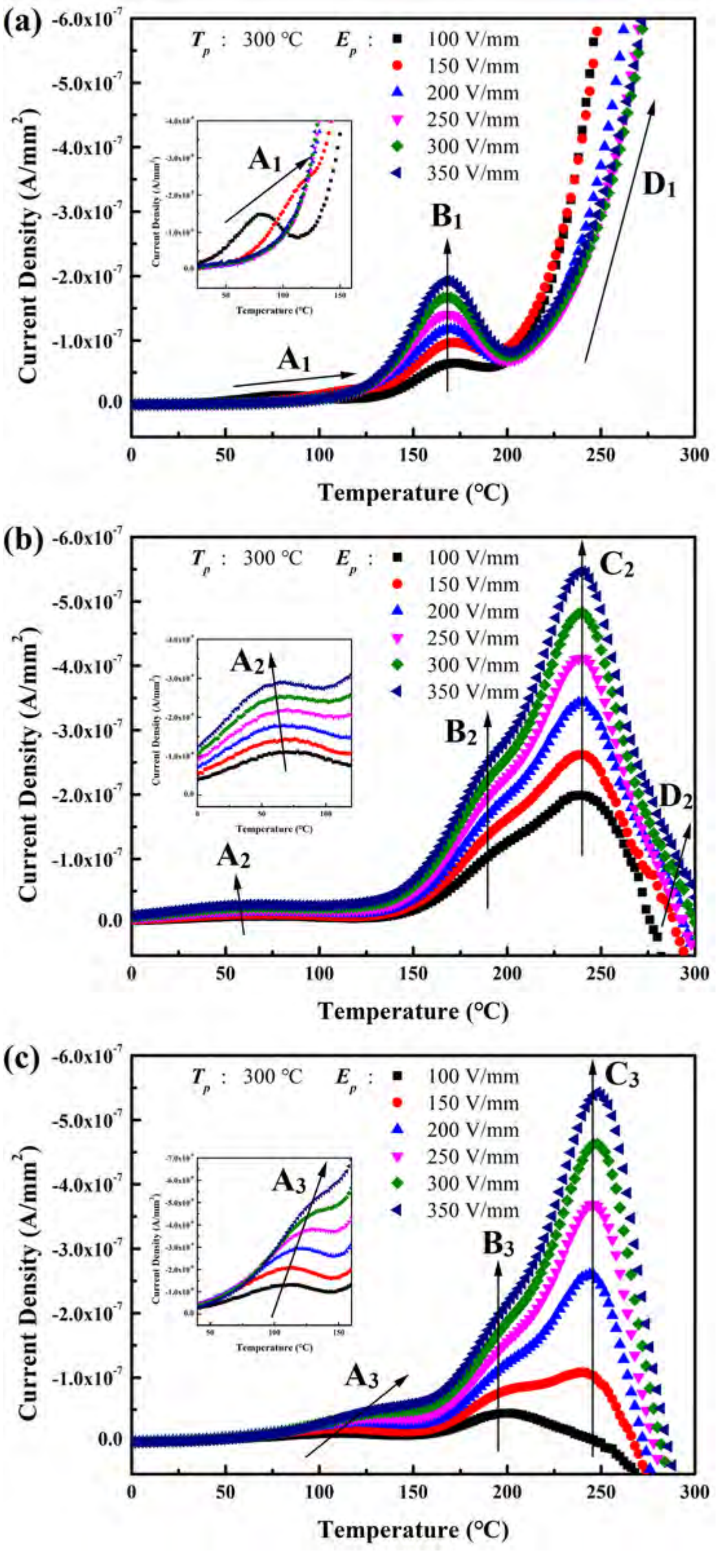

#### Figure 9

TSDC curves of (a) the BNT ceramics, (b) the BNT-A (z = 1.25) ceramics, and (c) the BNT-AN (z = 1.25) ceramics under Tp = 300 °C and 100 V/mm ≤ Ep ≤ 350 V/mm.

## Supplementary Files